Contents lists available at ScienceDirect

International Journal of Applied Earth Observation and Geoinformation

journal homepage: www.elsevier.com/locate/jag



InSAR-based assessment of post-earthquake building reconstruction: The Nepal case study

Fatemeh Foroughnia a^[], Valentina Macchiarulo a,b^[], Pietro Milillo c,d,e^[], Michael R.Z. Whitworth f^[], Kenneth Gavin a^[], Giorgia Giardina a^[]

- ^a Department of Geoscience and Engineering, Delft University of Technology, Stevinweg 1, Delft, 2628 CN, The Netherlands
- b ARGANS Ltd, Plymouth, United Kingdom
- c Department of Civil and Environmental Engineering, University of Houston, 4226 Martin Luther King Blvd, Houston, TX 77204, United States
- d Department of Earth and Atmospheric Science, University of Houston, 4226 Martin Luther King Blvd, Houston, TX 77204, United States
- e Microwaves and Radar Institute, German Aerospace Center (DLR), Münchener Straße 20, Weßling, 82234, Germany
- f AECOM, Tailyour Road, Plymouth, PL6 5DH, United Kingdom

ARTICLE INFO

Keywords: Earthquake Post-earthquake assessment Building reconstruction Field survey Remote sensing (RS) Synthetic Aperture Radar (SAR) Multi-Temporal SAR Interferometry (MT-InSAR)

ABSTRACT

Evaluating long-term building reconstruction is essential to strengthen resilience to earthquakes. Field investigations provide detailed and accurate information for building assessments, but are often labour intensive, costly, and time consuming, particularly when considering the regional-scale impact of earthquakes. In contrast, satellite Remote Sensing (RS) techniques provide frequent data across vast areas, making them ideal for regional-scale post-earthquake assessments, which can complement field surveys. Despite this, most RS studies have relied on manual change detection of satellite data before and after the event, limiting their potential for automated assessment and reducing their support for field investigations. In this study, we developed a novel RS method designed to assist field investigations of post-earthquake building reconstruction on a regional scale. The method automatically identifies target buildings for field teams to investigate, locating collapsed structures or buildings that have changed due to post-earthquake reconstruction efforts. We applied Multi-Temporal Synthetic Aperture Radar Interferometry (MT-InSAR) for the first time to evaluate post-earthquake building reconstruction. The proposed method involves a two-stage analysis; first, a grid-level assessment on a regional scale to detect areas with reconstruction activities following an earthquake, and then a detailed building-level analysis to identify individual buildings that have undergone changes as part of the reconstruction process within these areas. The method was used to assess building reconstruction efforts in Nepal after the 2015 Gorkha earthquake. For the MT-InSAR analysis, we acquired two stacks of 3-m-resolution SAR images, one before and one after the earthquake. The grid-level analysis detected multiple urban areas with significant changes, which were then subjected to a building-level analysis. This analysis pinpointed the locations of affected buildings and determined the extent of changes related to reconstruction activities. A comparison of the building-level results with field observations confirmed that the method successfully identified buildings that have undergone changes. These changes included buildings that were left in a collapsed state, demolished, under construction, or fully reconstructed. The MT-InSAR-based approach introduced in this study has the potential to serve as a valuable tool to guide future field surveys related to post-earthquake reconstruction, significantly reducing the time and effort needed for such assessment.

1. Introduction

Earthquakes are among the most destructive hazards, often causing extensive building damage and collapses, and resulting in significant loss of life. In recent years, many urban areas around the world have been affected by earthquakes. For example, the 2010 Haiti earthquake resulted in over 200,000 deaths and destruction of approximately

250,000 residences and 30,000 commercial buildings (Green and Miles, 2011), with damage and losses exceeding \$7.8 billion (Government of the Republic of Haiti, 2010). More recently, the 2023 earthquake in Turkey caused over 53,000 fatalities, 100,000 injuries, and widespread building damage, with losses estimated at \$84.1 billion (Aktas et al., 2024). As populations continue to grow, the consequences of such

E-mail address: f.foroughnia@tudelft.nl (F. Foroughnia).

^{*} Corresponding author.

disasters may become even more severe. This highlights the critical need for effective post-earthquake management and disaster risk reduction strategies in earthquake-prone areas. A crucial component of these efforts is assessing the building reconstruction process following an earthquake (Ge et al., 2010; Hashemi Parast, 2017).

Post-earthquake reconstruction of buildings involves repairing, reinforcing, or demolishing and rebuilding damaged structures (Polese et al., 2018). Typically, this process begins a few months after the earthquake and can last several years (Lu and Xu, 2015; Polese et al., 2018). For example, the reconstruction process was still in progress in Bam, Iran, six years after the 2003 earthquake (Omidvar et al., 2010). During the reconstruction process, there is an opportunity to identify and address structural weaknesses, such as poor quality materials, that prevent the ability of buildings to withstand earthquakes (Ahmed, 2017). By doing so, it is possible to mitigate risks that could compromise the resilience and sustainability of future buildings, ensuring safer and more resilient structures (Lyons et al., 2010). Assessment of the reconstruction process ensures that the process aligns with the established recovery strategy and plans (Clinton, 2006; Mannakkara et al., 2014). Additionally, it helps gather lessons to improve future post-disaster management and reconstruction efforts (Mannakkara et al., 2014).

Conventional surveys have been widely used to evaluate the post-earthquake condition of buildings, including assessing their reconstruction progress (Acharya et al., 2022). These methods include building-by-building field inspections (Eghbali et al., 2020), household surveys, and interviews (Platt et al., 2020; Westoby et al., 2021). While these investigations provide detailed, context-specific data through direct physical observations of structural conditions, they require experts to manually collect information on site. As a result, these surveys are time consuming, labour intensive, and costly (Brown et al., 2012; Platt et al., 2016), making them impractical for assessing reconstruction progress across affected large areas. Consequently, there is a growing need to explore new methods for post-earthquake assessments that can cover extensive regions more efficiently, helping to enhance traditional field surveys by identifying priority locations.

One promising approach is satellite Remote Sensing (RS) technology, which enables the observation of the Earth's surface without the need for physical presence. RS techniques offer large coverage, cost effective, and frequent observations, making them well suited for regional-scale post-disaster assessments and thus supporting field investigations. Commonly used RS data include optical and Synthetic Aperture Radar (SAR) imagery. Optical satellites acquire data in visible and infrared light, as human eyes perceive it, making them suitable for visual interpretation (Ge et al., 2020). SAR uses microwave signals, offering imaging capabilities in all weather and at night (Bamler, 2000; Hanssen, 2001).

Most RS studies have focused on the early phase of assessment, particularly on damage evaluation (Al-Khudhairy et al., 2005; Brown et al., 2012; Anniballe et al., 2018; Giardina et al., 2023; Voelker et al., 2024; Macchiarulo et al., 2024) and immediate demolition (Brown et al., 2012; Kushiyama and Matsuoka, 2019). A smaller number of studies have focused on the later reconstruction phase. These studies have primarily used change detection approaches to identify alterations resulting from reconstruction activities. Change detection methods compare two or more satellite observations taken before and after an event, either at the pixel or object (e.g. buildings) level, to detect differences between pre- and post-event conditions. For example, Derakhshan et al. (2020) used a time series of medium-resolution Landsat optical data to monitor building reconstruction over several years following earthquakes in Christchurch, New Zealand, L'Aquila, Italy, and Bam, Iran. Their approach involved automating the classification of built-up areas using spectral indices, followed by change detection on the classified maps to assess changes in these areas. However, their analysis primarily focused on estimating the rate of change in total built-up areas rather than detecting changes at the individual building level. Consequently,

this method lacks the ability to pinpoint the specific locations of altered buildings, limiting its usefulness for guiding field surveys.

In contrast, other research has specifically focused on tracking changes at the individual building level. For instance, Bevington et al. (2010) evaluated post-earthquake reconstruction in Haiti four months after the 2010 earthquake using optical satellite data. They manually analysed changes in heavily damaged and collapsed buildings identified by the Global Earth Observation Catastrophe Assessment Network (GEO-CAN), classifying the reconstruction progress into four stages: unchanged, rubble removal, under construction, and rebuilding. Their findings indicated that the reconstruction process varied both temporally and spatially, with most buildings remaining unchanged. This suggested that many buildings required more time for reconstruction, highlighting the need for a long-term assessment, which their study did not cover. Other studies have focused on conducting extended evaluations of post-earthquake building reconstruction using RS techniques. For example, Hashemi Parast et al. (2017) evaluated the reconstruction progress in Bam, Iran, after the 2003 earthquake using three highresolution optical images, one taken before, one immediately after and one eight years after the earthquake. They manually classified land cover within small regions to track changes in buildings over the eight-year period. Similarly, Contreras et al. (2018) assessed buildinglevel reconstruction following the 2009 L'Aquila earthquake. They used manual and semi-automatic change detection methods (Contreras et al., 2016), analysing classified maps of buildings from optical satellite data acquired in 2009 and 2011 to identify changes in individual buildings' conditions during the reconstruction process. While these studies have focused on building-level assessment, their approaches rely heavily on expert manual interpretation, resulting in high time and labour costs.

In a different approach, Hoshi et al. (2014) conducted an automated assessment of building-level reconstruction using machine learning, specifically the Maximum Likelihood classification method, to identify change patterns in buildings in Pisco from 2007 to 2011 after the 2007 Peru earthquake. This method detected changes in the ratios between buildings and vacant areas. However, advanced machine learning classifications depend on training models with sample data collected from ground-truth sources (Matin and Pradhan, 2022; Jia and Ye, 2023). Gathering these sample data still requires field investigations, which are time consuming and challenging to perform comprehensively, often leading to unbalanced training sets. Additionally, models trained on one dataset cannot always be generalised to other case studies, as differences in building features or environmental conditions can limit their applicability (Matin and Pradhan, 2022; Jia and Ye, 2023).

A well-established method that provides building-level information is Multi-Temporal Interferometric SAR (MT-InSAR), which uses stacks of SAR images. Thanks to the all-weather image acquisition capability of SAR sensors and their ability to cover large areas with short revisit times (Macchiarulo et al., 2024), MT-InSAR can monitor extensive regions affected by earthquakes using frequent SAR data. Additionally, high-resolution SAR data can be freely available through open data programs (ESA, 2024), making it well suited to accurate building-level assessments (Macchiarulo et al., 2024). The MT-InSAR technique identifies stable points, known as Persistent Scatterers (PSs), by analysing stacks of SAR images taken over time from the same area. These PSs typically correspond to man-made objects such as buildings, enabling detailed monitoring of changes at the building level. MT-InSAR has been widely used for long-term displacement monitoring in urban areas (Ciampalini et al., 2014; Bianchini et al., 2015; Foroughnia et al., 2019). However, no study has yet explored this technique to assess post-earthquake building reconstruction, nor has it been utilised to support field investigations.

In this research, we aim to develop a novel MT-InSAR-based tool to support post-earthquake field investigations by assessing building reconstruction progress, including buildings left in a collapsed state, demolished, under construction, or reconstructed. Compared to the use of image-based change detection methods relying on a single

pre-event image and long-term post-event imagery, this approach leverages a time series of SAR data to better capture the gradual and location-specific nature of reconstruction. MT-InSAR enables continuous monitoring of structural changes by detecting variations in PSs associated with buildings over time. This allows for automated identification of demolition, collapse, or reconstruction without the need for supplementary datasets, offering a more robust and targeted method for tracking post-disaster building reconstruction. The proposed method can guide field surveys by automatically identifying the locations of buildings that have changed from their pre-event state due to reconstruction efforts or that are still collapsed years after an earthquake. This approach provides target locations for field teams to investigate, significantly reducing the time and effort required for on-site assessments.

The proposed method was used to assess building reconstruction in Nepal following the 2015 Gorkha earthquake. Stacks of high-resolution Cosmo-SkyMed (CSK) SAR images were acquired before and after the earthquake for the MT-InSAR analysis. PSs associated with buildings were identified for both pre- and post-event time frames. A two-stage PS differential analysis was then conducted to locate buildings that had undergone changes. First, a grid-level analysis was performed to determine urban areas that showed significant changes, representing zones of extensive damage or active reconstruction. Second, a building-level PS differential analysis was conducted within these areas to pinpoint specific buildings affected by reconstruction activities. This building-level analysis not only identified the locations of these buildings but also assessed the extent of the changes. Results were validated using field observations collected during reconnaissance missions.

2. Methodology

This section describes the MT-InSAR technique, the parameters used to generate PSs, and the PS differential analysis developed in the study. The proposed method is based on the principle that a PS will cease to persist if changes occur to its corresponding target, such as collapses or modifications. Using this concept, the study applies a grid-level PS differential analysis on a regional scale, along with a building-level analysis, to detect significant changes and identify building locations with substantial changes, such as collapse, demolition, or reconstruction.

2.1. Multi-Temporal Synthetic Aperture Radar Interferometry (MT-InSAR)

MT-InSAR is an advanced remote sensing technique that uses the temporal phase information of SAR data to measure ground surface displacements (Ferretti et al., 2001). The core objective of MT-InSAR is to identify PSs, which consistently return strong backscatter signals to the satellite and show stability in phase over time (Ferretti et al., 2001), typically corresponding to natural features like rocks or manmade structures like buildings. The MT-InSAR technique uses a stack of SAR images to identify PSs.

To initiate this process, a primary set of points is selected as PS Candidates (PSCs) based on their amplitude stability. This stability is quantified using the Amplitude Dispersion Index (ADI), estimated as:

$$ADI = \frac{\sigma_A}{m_A} \simeq \sigma_v,\tag{1}$$

where σ_A is the amplitude standard deviation, m_A is the mean amplitude, and σ_v is the phase standard deviation of the SAR data stack. A point is chosen as a PSC if its amplitude consistently exceeds a defined threshold. Ferretti et al. (2001) proved that assuming sufficient data images, ADI below 0.25 indicates sufficient point stability and a high signal-to-noise ratio.

Once the PSCs are selected, SAR interferometry is used to estimate their displacements. MT-InSAR compares the interferometric phase between a primary image and secondary SAR images of the stack, acquired at different times over the same area. The interferometric phase consists of different components: displacement, topography, atmosphere, the Earth's curvature, and noise (Hanssen, 2001). To isolate the displacement component, other phase components are removed, as detailed by Ferretti et al. (2001), Perissin and Wang (2011) and Van Leijen (2014). The effects of Earth's curvature and topography are corrected using orbital data and an external Digital Elevation Model (DEM). Depending on the DEM's accuracy, a residual amount of topography effect may remain in the interferometric phase, which is later estimated with displacements. The atmospheric effect, known as Atmospheric Phase Screen (APS), is removed based on a two-step procedure. First, a temporal low-pass filter is applied to the residuals to separate unmodeled displacement (temporally correlated) from the atmospheric signal and noise, which are uncorrelated in time. Second, a spatial low-pass filter is used to extract the spatially correlated atmospheric signal from the remaining residuals, effectively isolating and removing the APS (Van Leijen, 2014). After the APS removal, a second set of PSs is selected using a higher threshold on ADI. Displacements are then re-estimated for all PSs. The amount of remaining noise in the interferometric phase per PS is used to calculate the Temporal Coherence (TC) as a reliability metric. Higher TC values indicate more accurate and stable PS estimates, ensuring the reliability of the analysis.

In this study, the MT-InSAR processing was performed using the SARPROZ software (Perissin et al., 2011). Although displacement measures were not the primary focus, the complete MT-InSAR process was crucial to identify reliable PSs corresponding to buildings. To select PSCs, we applied a threshold on the Amplitude Stability Index (ASI), implemented in the software as 1– *ADI*. Specifically, ASI values above 0.8 were used in the first processing stage and then reduced to 0.6 for the final PS selection. Only PSs with a TC higher than 0.7 were considered valid for the PS differential analysis. These thresholds are commonly adopted in standard MT-InSAR approaches, as established in the literature (Ferretti et al., 2001; Macchiarulo et al., 2021; Wu et al., 2022). The following section outlines the PS differential analysis developed in this study to assess building reconstruction.

2.2. Persistent Scatterer (PS) differential analysis

During seismic events, buildings that have been damaged or collapsed stop exhibiting the characteristics of PSs. Normally, an undamaged building maintains a consistent signal to the satellite over time. However, after an earthquake, a severely damaged or collapsed building exhibits irregular and disrupted signals. This disruption occurs because the building either no longer exists in its original form or undergoes further demolition and reconstruction, preventing it from being tracked as a PS. We leveraged this property of PSs to detect changes in buildings, first at a grid level and then at the level of individual structures, as shown in Fig. 1.

The grid-level analysis aims to identify urban areas that have undergone significant changes in the years following an earthquake. These areas can be prioritised for further evaluation to locate changed buildings through the building-level PS-differential analysis. To perform the grid-level analysis, we divided the area of interest into $100\times100~\text{m}^2$ grid cells. Within each grid cell, we quantified the number of PSs derived from pre- and post-event time-series images processed using MT-InSAR analysis. The difference in PS numbers at the grid level was determined by subtracting the post-event PS count from the pre-event PS count.

To identify grid cells with significant changes in PS numbers, we normalised these differences using a representative number of PSs from the entire area of interest obtained from the pre-event series (Eq. (2)). This process involved dividing the number of pre-event data points within each grid cell into equal quartiles and excluding the outliers. The normalisation was based on the upper bound (*UB*) of the distribution of the number of PSs within each grid cell (from the pre-event data),

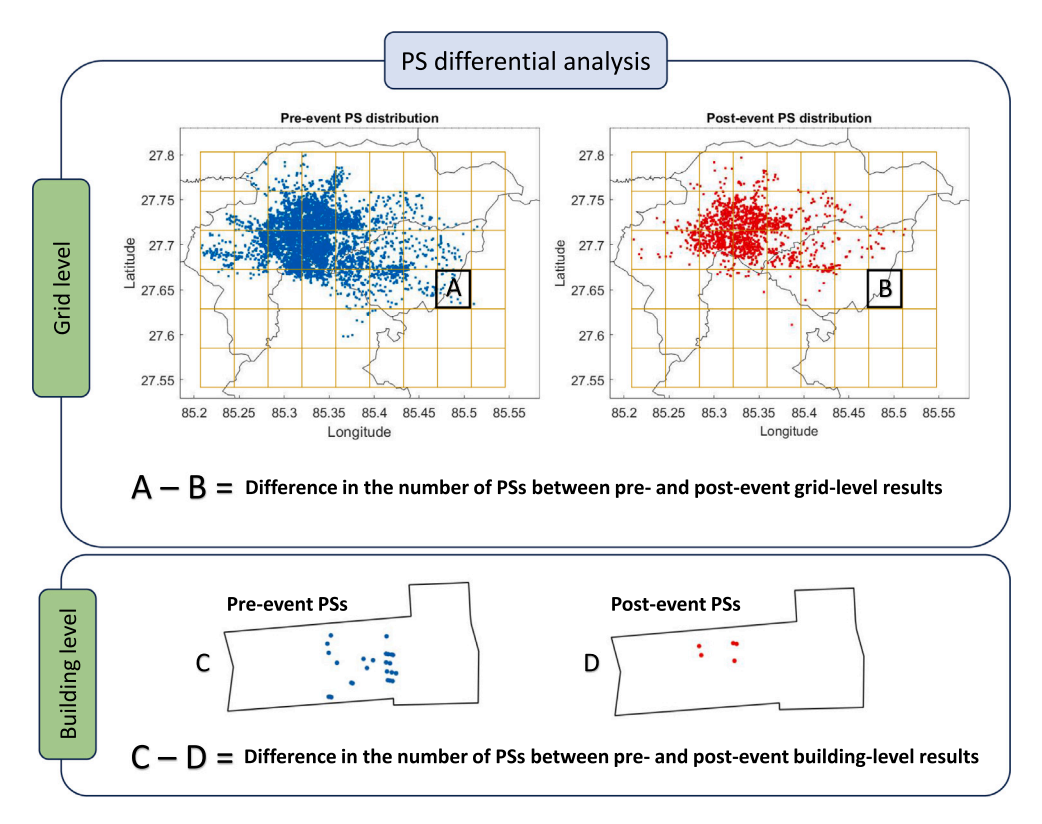


Fig. 1. Schematic representation of the PS differential analysis at grid and building levels.

defined as the largest data point excluding the outliers, and estimated as follows:

$$UB = Q_3 + 1.5 * (Q_3 - Q_1)$$
 (2)

where Q_1 represents the first quartile, which is the median of the lower half of the dataset, below which 25% of the data points fall. Similarly, Q_3 is the third quartile, the median of the upper half of the dataset, meaning that 75% of the data points fall below this value. This approach helps prevent the impact of outliers from skewing the analysis of PS differences. Fig. 10 in the Appendix Section illustrates the distribution of the number of PSs obtained from the pre-event time series and the parameter $UB\left(N_{\mathrm{pre}}\right)$. The differences in the number of PSs at the grid level, D_{Grid} , are then estimated as follows:

$$D_{\text{Grid}} = \frac{N_{\text{pre}} - N_{\text{post}}}{UB(N_{\text{pre}})},$$
(3)

where $N_{\rm pre}$ and $N_{\rm post}$ are the number of PSs identified in each grid from the pre- and post-event time series, respectively. $UB\left(N_{\rm pre}\right)$ refers to the upper bound of the number of points in the grid cells obtained from the pre-event time series. $D_{\rm Grid}$ indicates the relative change between the pre- and post-event conditions in each grid cell, compared to the other grid cells in the area of interest.

The grid-level analysis was designed to prioritise grid cells with more or larger buildings over those with fewer or smaller ones at equivalent levels of PS loss. Since larger buildings and a higher number of buildings typically generate more PSs (Ferretti et al., 2001; Hooper et al., 2004; Crosetto et al., 2016), this approach emphasises grid cells with more PSs when similar levels of PS loss are observed. Fig. 2 provides examples of how the grid-level analysis operates. A grid cell with more pre-event PSs and a certain percentage of point loss due to reconstruction will be prioritised over a grid cell with fewer pre-event PSs in case of the same percentage of point loss. For example, according to Fig. 2, and assuming $UB\left(N_{\rm pre}\right)$ is equal to 100 for simplicity, Grid 1 in the first example has 50 points and a 50% point loss (25 points disappeared), resulting in a 25% differential change. In contrast, Grid

2, with 26 points and 13 points disappeared, shows a 13% differential change. In other examples, where the percentage of point losses differ, the differential changes directly depend on the level of point losses. For example, in the same figure, Grid 2, even with 100% of point loss, exhibits less of a differential change (26%) than Grid 1 (40%) with 80% of point loss.

Importantly, the $100\times100~\text{m}^2$ grid resolution was chosen to balance spatial granularity with computational efficiency. The methodology remains robust across different grid sizes because it relies on a normalised change metric that adjusts for variations in the number of PSs per grid. The approach remains flexible and can be adapted to alternative grid configurations depending on specific research needs.

The outcomes of the grid-level analysis served as a guiding framework for performing a more detailed investigation at the building level. The building-level PS differential analysis identifies buildings that have undergone significant changes after the earthquake during the reconstruction process. These building-level changes can include structures that remain collapsed, have been demolished, are under construction, or are fully reconstructed. We conducted the PS differential analysis for buildings located in zones with high concentrations of grid cells exhibiting significant changes. Building footprints from the OpenStreetMap (OSM) database (OpenStreetMap, 2023) were used to quantify the presence of PSs within each building for both pre- and post-event data. The change in the number of PSs for each building was estimated by subtracting the number of PSs in the post-event data from the pre-event data. Similar to the grid-level analysis, the percentage of PS differences was normalised using the ratio between each building's area and the upper bound of the building area dataset, which acted as a weighting factor.

The percentage of PS differences at the building level, $D_{\rm building}$ was estimated as follows:

$$D_{\text{building}} = \frac{N_{\text{pre-bu}} - N_{\text{post-bu}}}{N_{\text{pre-bu}}} \times \frac{area_{\text{bu}}}{UB \left(area_{\text{bu}}\right)} \times 100, \tag{4}$$

where $N_{
m pre-bu}$ and $N_{
m post-bu}$ are the number of PSs identified from the pre- and pos-event time series for each building footprint, respectively,

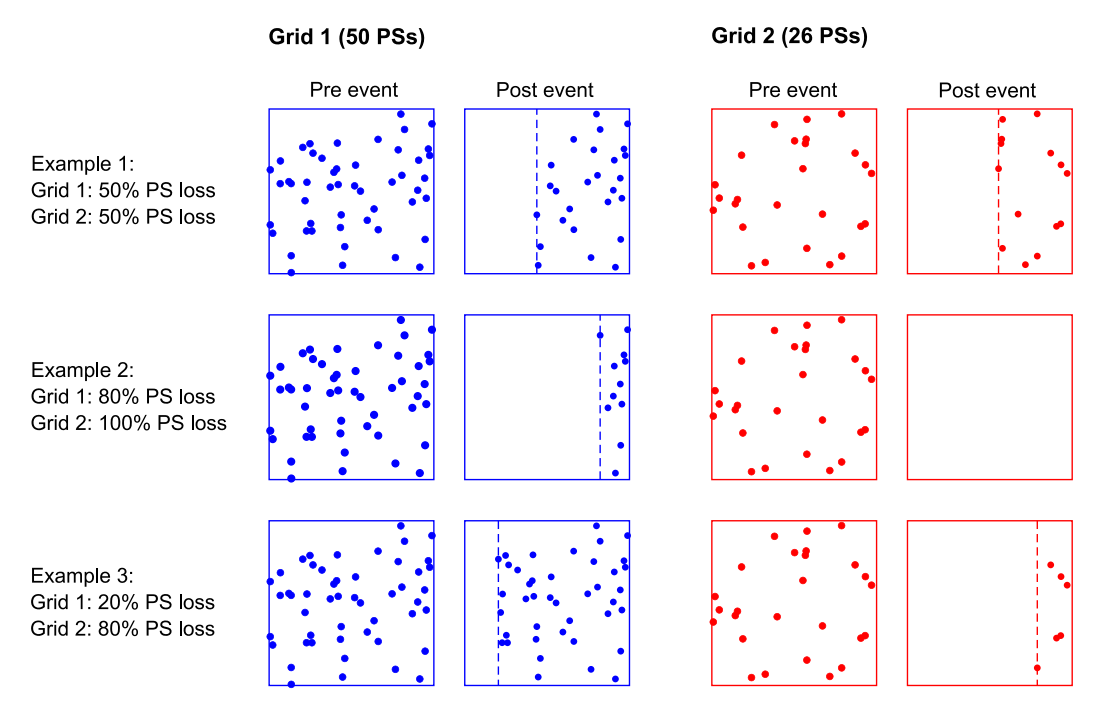


Fig. 2. Examples of grid-level differential analysis. In Example 1, 50% of points have disappeared in a denser grid cell due to reconstruction years after the earthquake. Example 2 shows an 80% point loss in Grid 1 compared to a 100% loss in Grid 2. In Example 3, 20% of points in Grid 1 and 80% in Grid 2 have disappeared. The analysis indicates more changes in the denser Grid 1 for Example 1, while in Examples 2 and 3, the differential changes depend on the degree of point loss in each grid.

 $area_{\rm bu}$ represents the area of each building rooftop, calculated using the OSM building footprints, and UB ($area_{\rm bu}$) is the upper bound of the building areas distribution (the largest value of areas without outliers) in the detected zones. Similar to the grid-level analysis, this upper bound was calculated based on Eq. (2), but using the size of buildings. The values of UB ($area_{\rm bu}$) used in this study are reported in Table 1 in Appendix.

The weighting factor ensures that larger buildings have a greater influence in terms of the magnitude of change associated with reconstruction. For example, a larger building unit will show a higher amount of D_{building} compared to a smaller building with the same normalised difference (as described in the first ratio in Eq. (4)). Additionally, for buildings with the same area, similar to the grid-level analysis, D_{building} depends entirely on the normalised difference, i.e. the percentage of PS point loss during the reconstruction process. This approach is based on the principle that larger buildings often represent high-value infrastructure and densely populated areas, which can be more critical to overall urban functionality than smaller buildings. By applying the weighting factor based on the area of the buildings, we ensure that larger buildings are given appropriate emphasis in the analysis. The weighting factor may vary depending on the case study considering specific purposes. For example, if residential buildings are of particular interest, smaller buildings may also be prioritised by defining a different weighting factor. This flexibility allows the method to adapt to different contexts and focus on the most relevant types of buildings.

3. Case study and datasets

On April 25, 2015, Nepal was struck by a moment magnitude (Mw) 7.8 earthquake. The epicentre was situated near Gorkha, approximately 80 km northwest of Kathmandu, the capital city. The earthquake occurred at a focal depth of 19 km (USGS, 2015), and its impact was extensive, resulting in widespread destruction in areas extending from the epicentre to the east, including Kathmandu. Many aftershocks followed the main earthquake, with the largest one occurring on May

12, 2015, recording a moment magnitude of Mw 7.3 (USGS, 2015). Both urban and rural areas suffered significant damage to buildings and infrastructure as a result of the main shock. By May 26, 2015, the earthquake's toll in Nepal included 8510 reported deaths and 199 missing people (Goda et al., 2015).

According to Lizundia et al. (2016), the earthquake caused extensive damage to residential and governmental buildings, heritage sites, schools, roads, bridges, water systems, and agricultural areas. Many ancient cultural buildings were severely damaged or destroyed, along with over 500,000 houses. The Center for Disaster Management and Risk Reduction Technology (CEDIM, 2015) estimated the economic loss to be around 10 billion U.S. dollars, which accounted for approximately half of Nepal's gross domestic product (Goda et al., 2015). Fig. 3 shows the selected region of interest, covering the most affected areas in 2015.

Remote sensing data. We used Single Look Complex (SLC) imagery from COSMO-SkyMed (CSK), an Italian constellation of SAR satellites dedicated to Earth imaging. The purpose of this constellation is to provide high-resolution SAR data within the X-band frequency range for various applications, including Earth observation, environmental monitoring, and disaster management (Italian Space Agency, 2019).

For this study, we collected two temporal series of SAR images in Stripmap mode before and after the event. The post-event time series started following the largest aftershock on May 12, 2015. All images were acquired from a descending orbit in HH polarisation with a minimum revisit time of four days and a spatial resolution of 3 m. The pre-event series included 30 SAR images acquired from June 2014 to January 2015. For the post-event series, we considered different time intervals with varying numbers of images to assess the impact of time series length on the differential analysis. These time intervals were selected to correspond to different phases of reconstruction activities. The shortest post-event time series begins nearly a year after the earthquake, when collapsed buildings may have entered the late stages of reconstruction, such as being under construction or fully reconstructed. The other two time series start closer to the earthquake date, also capturing the initial stages of reconstruction, such as debris removal and demolition. Fig. 4 shows the temporal distribution of the pre-event and

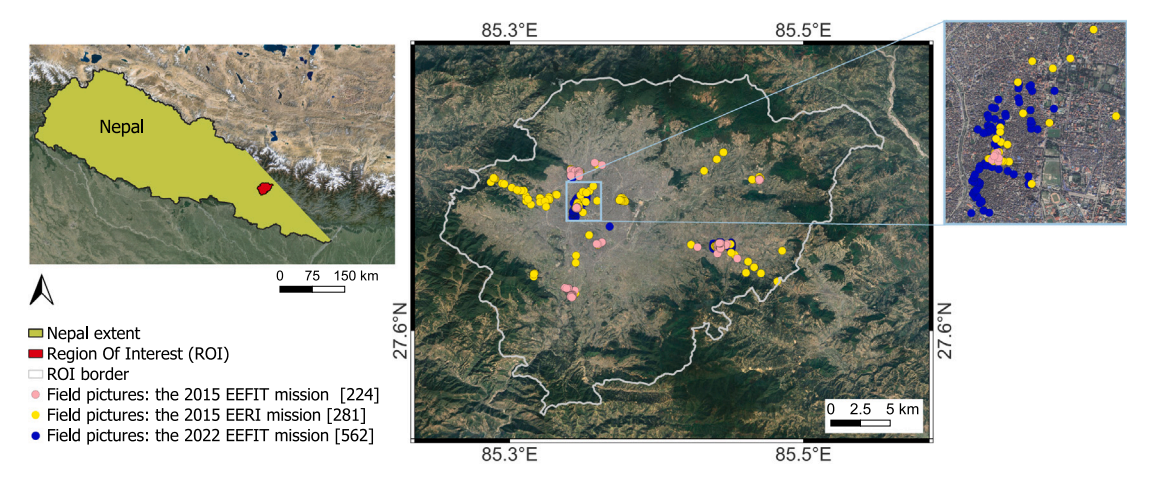


Fig. 3. A view of the region of interest, highlighting the locations where field pictures were taken. The close-up image on the right-hand side of the figure shows the distribution of these field pictures within Kathmandu. Google satellite imagery is used as a background layer. (For interpretation of the references to colour in this figure legend, the reader is referred to the web version of this article.)

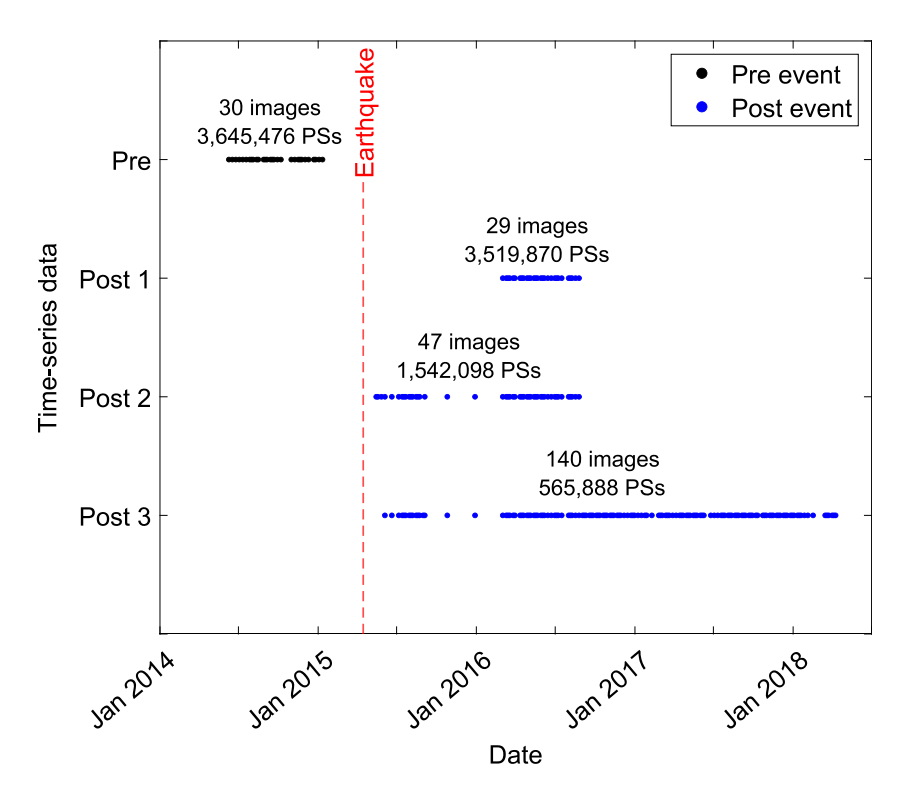


Fig. 4. Temporal distribution of CSK data images for the different time series before and after the earthquake. The detected number of PSs with Temporal Coherence higher than 0.7 is specified for each pair. (For interpretation of the references to colour in this figure legend, the reader is referred to the web version of this article.)

post-event time series. The post-event datasets, labelled 1 through 3, consist of 29, 47, and 140 images, respectively. SAR image acquisition dates with corresponding perpendicular and temporal baselines, and Doppler Centroid (DC) relative to the primary image of the post-event series number 2 are reported in Table 3 in Appendix.

Field data. To validate the results, we used field pictures collected by the Earthquake Engineering Research Institute (EERI) and the Earthquake Engineering Field Investigation Team (EEFIT) during their post-reconnaissance missions in 2015, as well as data from the 2022 EEFIT return mission.

EERI is a nonprofit technical society focused on advancing the science and practice of earthquake engineering. It actively contributes to post-earthquake reconnaissance efforts, conducting field investigations

to assess the performance of structures and infrastructure after seismic events (EERI, 2015). EEFIT is a collaborative initiative involving industry and academic institutions, dedicated to conducting comprehensive field investigations following significant earthquakes.

Two months after the 2015 Gorkha earthquake, EEFIT initiated a reconnaissance mission to investigate the earthquake's on-site impact (EEFIT, 2019). In May 2022, EEFIT returned to Nepal for a follow-up mission to gain insights into the country's recovery process and evaluate the effectiveness of the Build Back Better approach to disaster recovery (Whitworth, 2023). During their building assessments, the field team had two primary objectives: first, to verify any changes in structures affected by the earthquake, and second, to document the status of these buildings, noting the process of reconstruction efforts. Some of their observations were gathered in Kathmandu and Bhaktapur,

where a high level of damage was observed in 2015. The pictures they collected depicted various changes to buildings, including those that had remained collapsed, been demolished, were under reconstruction, or were newly constructed. The locations of the field pictures within the area of interest are represented in Fig. 3.

4. Results

The following sections present the results of the PS differential analysis conducted at both the grid and building levels, along with the validation of the identified buildings using field data.

4.1. Grid-level analysis

The MT-InSAR technique was applied to process one pre-event and three distinct post-event CSK datasets, as presented in Fig. 4. The figure also indicates the number of PSs with TC higher than 0.7 that were identified for each time series used in the PS differential analysis. Due to variations in the number of SAR images in the pre- and post-event time series, the number of PSs identified in each pair differs. This is explained by Eq. (1), which indicates that in a longer time series, the likelihood of a point undergoing changes (e.g., due to vegetation growth, construction, or other environmental factors) increases, reducing its stability as a PS. In our study, the varying time periods covered by each pair influence the temporal coverage of building reconstruction activities, which affects the number of PSs associated with buildings as they undergo physical changes. Hereafter, we label the pre- and post-event time-series pairs, each comprising the pre-event dataset paired with one of the post-event datasets, as Pairs 1, 2, and 3.

The outcomes of the PS differential analysis conducted at the grid level are illustrated in Fig. 5. This analysis provides a regional-scale overview of differences in PS numbers, highlighting significant spatial patterns of changes resulting from reconstruction activities years after the earthquake. Each point in the figure corresponds to a grid cell, with the colour indicating the magnitude of normalised differences between the pre- and post-earthquake PSs available for that grid cell. The variation in the number of PSs across different time series influences the level of PS changes observed between the pre-event and the three post-event situations. To effectively highlight areas with significant changes, we categorised the PS differences into three levels using different colour scales: green for small changes, yellow for moderate changes, and red for extensive changes. Due to the variation in the number of PSs across the different time-series pairs (Fig. 4) and the different patterns of change observed in each pair, the colour scales were adjusted individually for each pair. This approach ensures that the concentration of PS differences is accurately reflected for each period, allowing for a more meaningful comparison of changes across the various time-series pairs.

The results of the grid-level analysis revealed distinct spatial patterns in the distribution of PS differences across the study area (Fig. 5). The majority of grid cells were classified into the small change category, primarily located on the outskirts of urban areas. These regions experienced minimal alterations in PS point density, suggesting little to no reconstruction activities. Some grid cells exhibited moderate changes, indicating urban regions with moderate overall changes. For example, these changes can correspond to structures that suffered moderate damage during the earthquake, followed by moderate levels of repair and modification activities. A significant number of grid cells exhibited extensive changes, primarily in areas where buildings had partially or totally collapsed. These extensive changes in these regions could refer to structures that have collapsed and been demolished or structures with ongoing reconstruction activities years after the earthquake.

All pairs, except for Pair 1, show a consistent pattern of changes, with more changes observed in longer series. The extent of detected changes depends on the reconstruction activities during the periods

covered by each pair, with buildings showing SAR signal instability throughout reconstruction. For example, Pair 3 has the longest post-event time series, starting about 20 days after the major aftershock and continuing for nearly 3 years. This longer coverage captured more changes associated with long-term reconstruction activities within the area of interest. The extended reconstruction efforts led to a significant reduction in the number of PSs, resulting in a greater number of grid cells showing extensive PS differences. This can be due to the gradual modification of collapsed buildings over time, including debris accumulation, debris removal, demolition, and reconstruction. While short gaps between acquisitions could potentially miss rapid reconstruction activities, the overall trend in PS loss still provides a robust indication of reconstruction dynamics.

In contrast, Pair 1, which has the shortest post-event time series, showed a different pattern of changes than the other longer series in the grid-level analysis (Fig. 5(a)). This is likely because the post-event time series for Pair 1 started roughly a year after the earthquake and included fewer SAR images (Fig. 4). As a result, there is a notable gap in data from the critical period immediately following the earthquake to one year later, possibly leaving reconstruction activities unrecorded. Any changes during this one-year gap are not reflected in the time series, limiting the understanding of building conditions. Additionally, shorter time series with fewer SAR images are less capable of capturing gradual reconstruction-related changes.

Fig. 5 shows that extensive levels of changes are widely distributed across urban areas, with some zones having more grid cells exhibiting extensive changes. In particular, two such zones are located in central Kathmandu and Bhaktapur, as indicated by the black rectangles in Figs. 5(b) and 5(c). These zones were among the areas most severely affected by the earthquake, as confirmed by the field investigations conducted in 2015 (Wilkinson et al., 2019). Consequently, these zones were selected for a more detailed building-level analysis, as described in the next section.

4.2. Building-level analysis

The PS differential analysis at the building level was performed in urban zones (Fig. 6a) where a significant number of grid cells exhibited extensive changes, as a result of the grid-level analysis described in the previous section.

The distribution of the number of PSs within building footprints from the pre-event and the longest post-event time series is presented in Fig. 11 in Appendix. As a result of changes in the physical condition of buildings after the event, the number of PSs detected post-event decreased. Fig. 6 shows the outcomes of building-level PS differential analysis for the zones indicated, using Pair 3. The percentage of PS differences between the pre- and post-event time series was calculated for buildings within the selected zones. These PS differences were categorised into three levels of change, using consistent intervals across all categories. Different colours were used to represent varying levels of changes at the building level. Green represents a small percentage of changes, ranging from 0% to 33%, indicating minimal variations in PS point density associated with the building and suggesting stable building conditions with little to no reconstruction activities. Yellow indicates moderate changes, between 33% and 66%, corresponding to buildings that likely experienced moderate damage during the earthquake or have undergone some level of repair or modification. Red, representing changes above 66%, indicates extensive alterations, signifying buildings that likely suffered severe damage and are either undergoing significant reconstruction or remained damaged or collapsed. The division of the 0%-100% range into equal intervals was selected solely for visualisation purposes. Fig. 6 shows that three years after the earthquake, 58.11%, 29.55%, and 12.34% of the buildings within the regions of interest have experienced small (0% $\leq D_{\text{building}} <$ 33%), moderate (33% $\leq D_{\text{building}} < 66\%$), and extensive ($D_{\text{building}} \geq$ 66%) changes, respectively.

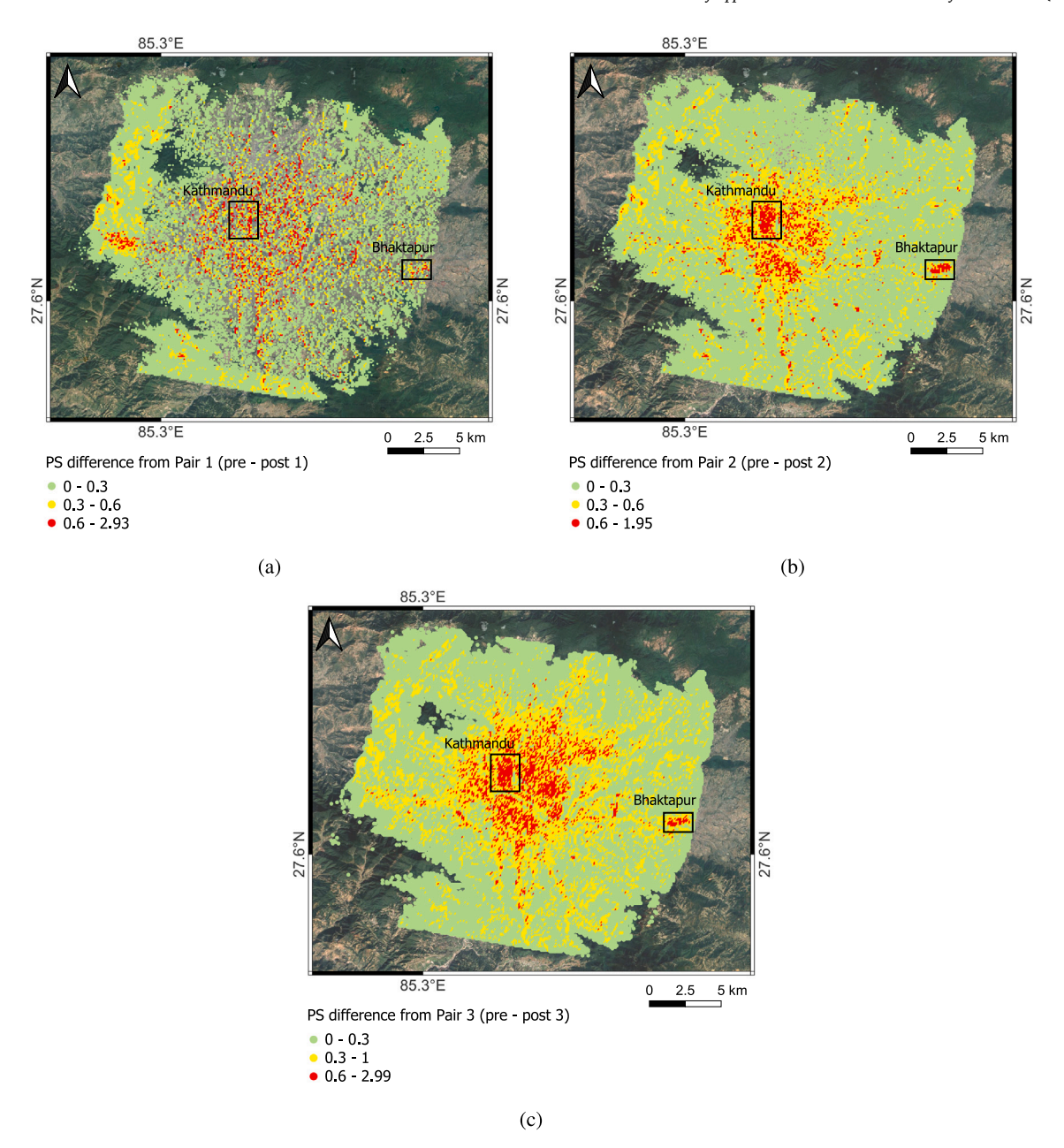


Fig. 5. Results of PS differential analysis on the regional scale in Nepal from (a) Pair 1, (b) Pair 2, and (c) Pair 3. Different colour scales were used to highlight the concentration of changed areas in the maps separately. The black rectangles show areas with a high concentration of grid cells with extensive changes, linked with two main affected areas in 2015, one in Kathmandu and one in Bhaktapur.. (For interpretation of the references to colour in this figure legend, the reader is referred to the web version of this article.)

4.3. Validation of building-level results

We validated the building-level results using pictures taken by the EEFIT and EERI teams during the 2015 post-event reconnaissance mission and by the EEFIT team during the 2022 return mission. From the 2015 missions, only images of severely damaged or collapsed buildings were selected for validation, as those were the buildings expected to undergo reconstruction. A total of 115 and 59 field pictures were chosen from the 2015 EERI and EEFIT missions, respectively. Additionally, 531 pictures of collapsed, demolished, under-construction, or newly constructed buildings were used from the 2022 EEFIT mission. A total number of 152 and 553 pictures were used for validating the results from Kathmandu and Bhaktapur, respectively.

For the validation, we extracted buildings with a relevant level of changes by applying a threshold to the percentage of PS differences at the building level. Specifically, buildings with a PS difference percentage (D_{building}) greater than 50% were selected for validation. The number of identified buildings is reported in Table 2 in the Appendix Section. To associate each field picture with a specific building, we applied a buffer zone of 25 m around the location of each picture. If multiple pictures were taken of the same building, the average location of those pictures was used. The 25-m buffer accounted for potential errors, such as the Global Positioning System (GPS) accuracy of the camera for picture locations and the distance between the surveyor and the building being photographed. A picture was considered to correspond to a building if its buffer zone intersected with the building's footprint. This counted as one positive correlation between the picture and the building, indicating a match between the method's identified buildings and the field observation. In cases where a picture intersected with multiple buildings, only one positive correlation was considered to ensure that each picture was associated with a single building.

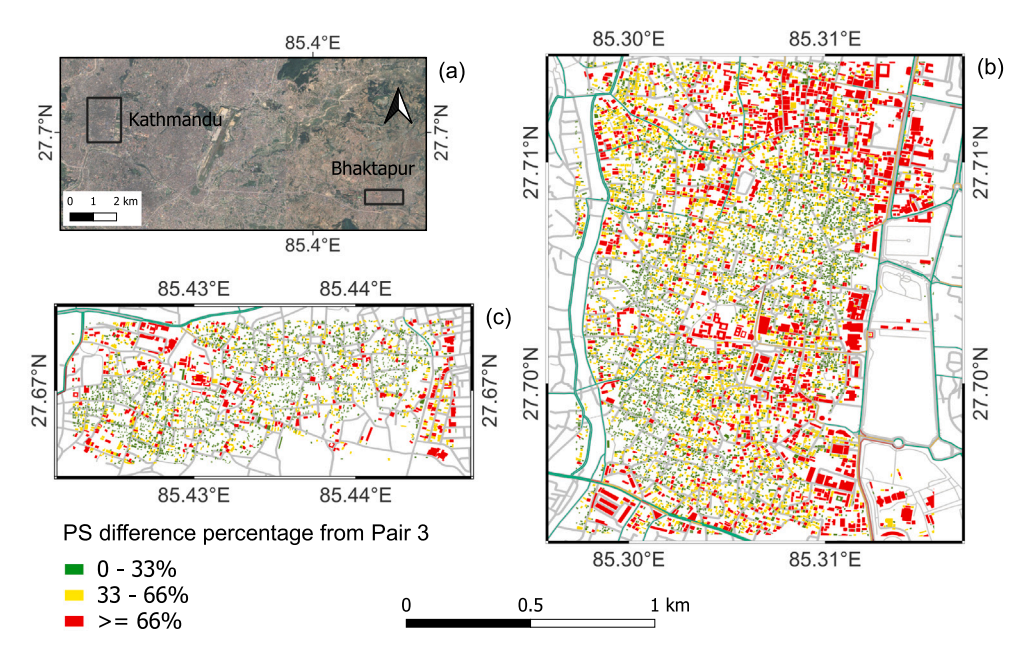


Fig. 6. Building-level PS differential results using Pair 3 across (a) two identified areas: (b) Kathmandu and (c) Bhaktapur. (For interpretation of the references to colour in this figure legend, the reader is referred to the web version of this article.)

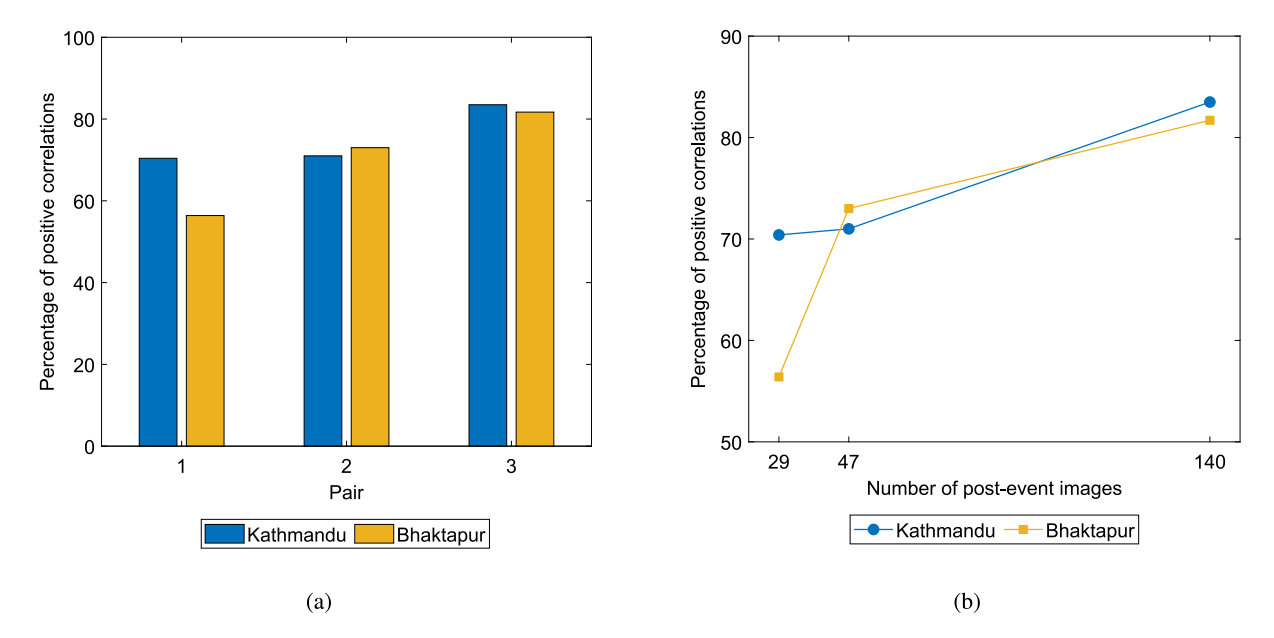


Fig. 7. Accuracy of the building-level results: (a) histogram showing the percentage of positive correlations between field pictures and buildings with over 50% changes per pair and (b) line graph showing the percentage of positive correlations between field pictures and buildings with more than 50% changes, based on varying numbers of post-event images for Kathmandu and Bhaktapur.. (For interpretation of the references to colour in this figure legend, the reader is referred to the web version of this article.)

The accuracy of the results was evaluated based on the percentage of correlation between the detected buildings that underwent reconstruction activities and the number of validation pictures. To obtain this, for each area, we calculated the ratio of positive correlations to the total number of validation pictures within the specific regions of interest. Fig. 7 illustrates the estimated accuracy of the building-level results for each area i.e., Kathmandu and Bhaktapur, using all pairs. Fig. 7(a) shows the percentage of positive correlations per region and per pair. Additionally, Fig. 7(b) illustrates the relationship between the accuracy of the building-level results and the duration of the postevent time series. In this graph, the X-axis represents the post-event image numbers, while the Y-axis shows the percentage of positive correlations.

The validation results revealed an increasing trend in the percentage of positive correlation across all regions as we progress from Pair 1 to Pair 3. The results from Pair 1, including the shortest post-event series, had fewer matches between the pictures and the buildings with more than 50% changes, resulting in correspondence rates between 56% and 70%. Conversely, Pair 3, which included the longest post-event time series, closely correlated with field observations, with matching rates from 81.7% to 83.5%. This confirms that longer post-event InSAR series are more effective at identifying buildings experiencing significant changes within the regions. The longer the post-event time series, the more building condition changes related to reconstruction activities are captured. As a result, more PS losses are detected in the longer time series. Furthermore, in a longer series of SAR images, coherent signal

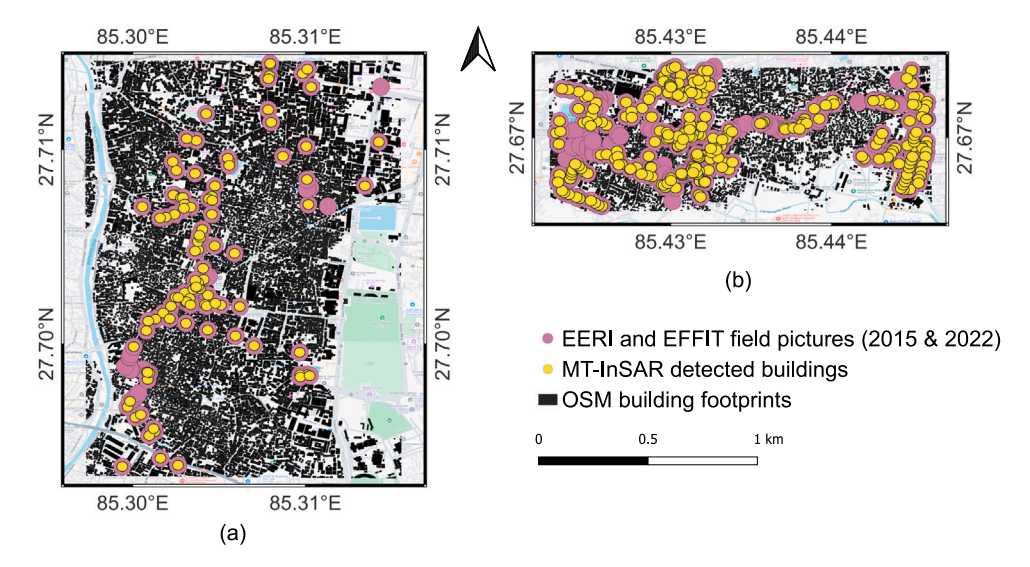


Fig. 8. Distribution of the detected buildings, which were in agreement with field pictures for areas (a) Kathmandu and (b) Bhaktapur. (For interpretation of the references to colour in this figure legend, the reader is referred to the web version of this article.)

and incoherent noise components of the SAR data can be separated more effectively. This improves the signal-to-noise ratio and enhances the ability to detect changes in the scattering properties of buildings, resulting in a more accurate detection of PSs (D'Aria et al., 2009), and leading to better identification of changes related to building reconstruction. The distribution of buildings with more than 50% changes, along with the distribution of field observations, is shown in Fig. 8.

Fig. 9 shows examples of field observations that positively correlated with buildings with more than 50% changes. The figure also illustrates the footprint of a reconstructed building with the corresponding PS loss. These positive correlations confirm that the buildings identified by the proposed method as experiencing high levels of change correspond to those observed in the field as undergoing significant post-earthquake modifications. The figure illustrates that the detected buildings are correctly associated with structures that were demolished, under construction, reconstructed, or remain collapsed.

5. Discussion

This study develops a new remote sensing approach that identifies reconstruction areas on a regional scale, followed by a detailed analysis at the individual building level. The building-level analysis identifies the locations of structures that have undergone changes due to reconstruction, particularly those heavily damaged during an earthquake and likely to have been reconstructed afterwards.

To date, no studies have developed a tool specifically designed to support field surveys to assess building reconstruction. As confirmed by the validation results, this approach provides a valuable method for guiding field investigations related to post-earthquake assessments of building reconstruction, allowing on-site surveys to focus solely on identified locations. By pinpointing specific buildings, the tool facilitates more cost-effective, timely, and targeted field data collection during reconstruction assessments. In practical terms, identified building locations can be directly imported into a surveyor's mobile phone application, enabling surveyors to effectively track and visit each building individually. This streamlines the field investigation process by reducing the workload and time required to manually identify target areas. The status of building reconstruction, i.e. buildings that remain collapsed, or were demolished, reconstructed or newly built, can be classified during the field survey.

A comparison between the proposed method and traditional field survey approaches highlights the significant efficiency gains in terms of time and human resources. Specifically for this study, the proposed method, which includes SAR data processing and PS differential analysis, required 32 h in total, equivalent to 4 working days for a single person, to analyse 12 387 buildings. In contrast, traditional field investigations are far more resource intensive. For instance, the post-earthquake reconnaissance of 5790 structures in rural Turkish villages took 5 days, requiring multiple teams (Livaoğlu et al., 2018). Similarly, Goretti and Di Pasquale (2004) reported that the standardised assessment of 23,000 buildings took 60 days and involved 100 inspection teams, amounting to approximately 80,000 person-hours. This comparison clearly demonstrates that the proposed InSAR-based approach offers a scalable and efficient alternative for the assessment of post-disaster building reconstruction.

The implementation of the proposed method requires a time series of high-resolution SAR imagery data acquired before and after an earthquake. High-resolution data is essential for individual building assessments (Miura et al., 2016; Macchiarulo et al., 2024), particularly when the case study includes small buildings. In this study, we used X-band CSK data with a 3-m-resolution cell size, capturing PSs associated with both small and large buildings within the area of interest. The CSK data demonstrated good performance, successfully identifying buildings of various sizes and reflecting their reconstruction conditions, as shown in Fig. 6.

The results highlight the importance of carefully selecting the post-earthquake time series period to effectively capture the full dynamics of reconstruction. Pair 1 did not provide reliable insights, as its post-event time series began a year after the earthquake and covered only five months. As a result, both the early structural changes and much of the subsequent reconstruction activity were missed. For effective monitoring, the post-event time series should ideally start shortly after the disaster, and include at least 20 to 25 images (Colesanti et al., 2003; Crosetto et al., 2016), which is generally considered the minimum required for reliable PS detection. Depending on the specific event and the pace of reconstruction, the time series should be extended as much as possible to fully capture all phases of the reconstruction process.

The method is inherently robust against environmental factors, such as vegetation growth, seasonal surface changes, or unrelated infrastructure modifications and is particularly given its focus on persistent, long-duration changes indicative of post-earthquake reconstruction. These effects are relatively minor compared to the significant structural changes associated with building demolition or reconstruction. At the

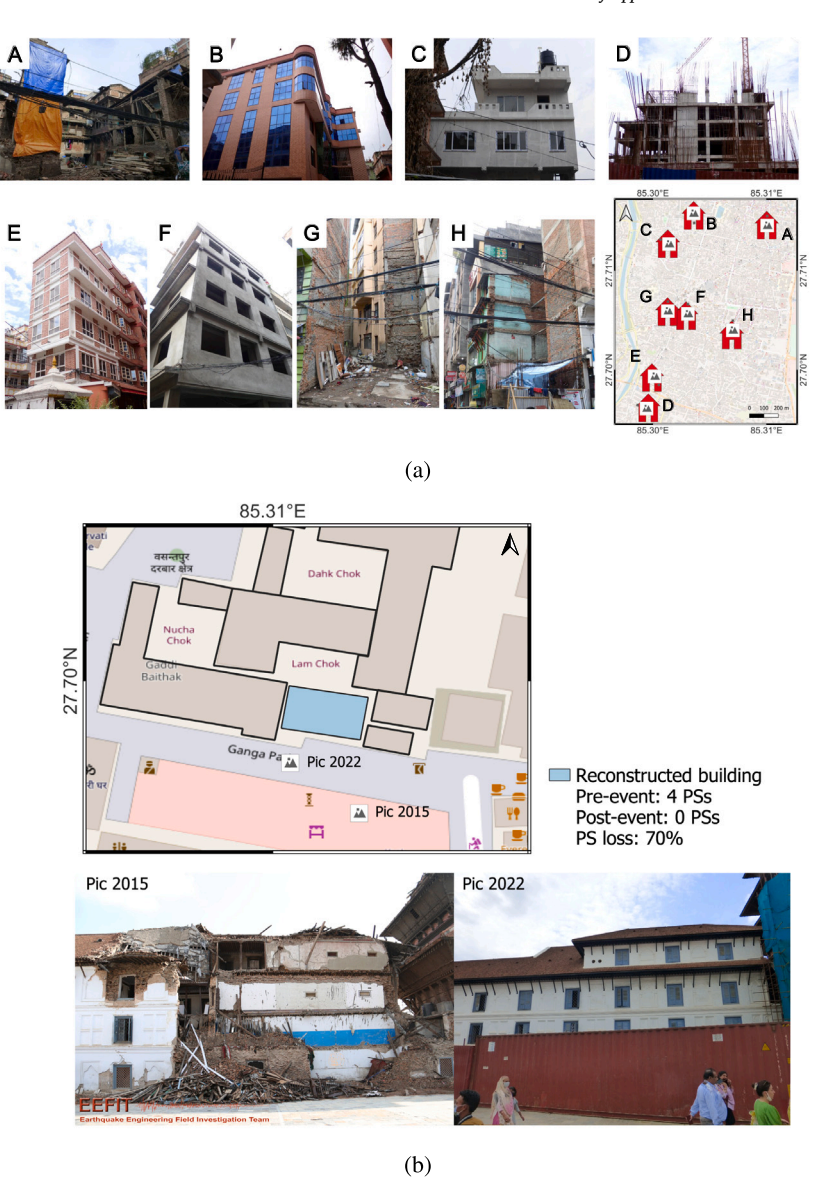


Fig. 9. Examples of surveyed buildings from the 2022 EEFIT mission that correspond to buildings with over 50% change. In (a) Figures A, G, and H correspond to demolished buildings; B, C, and E show reconstructed buildings; and D and F show buildings under construction. (b) An example of a reconstructed building in Kathmandu, showing the building footprint, corresponding field pictures, and the percentage of PS loss.

regional scale, MT-InSAR primarily captures signals from stable, reflective surfaces like buildings, minimising the influence of environmental noise. At the building level, the footprint-based approach further ensures that PS points are directly linked to the structure itself, reducing the likelihood of interference from surrounding vegetation or surface conditions.

It is important to acknowledge that the proposed method involves certain uncertainties. The validation results highly relied on the accuracy of the camera's GPS, which was used to determine the location of the on-site pictures. The median horizontal error of high-sensitivity embedded GPS hardware of mobile phones is reported between 5 and 8.5 m (Zandbergen and Barbeau, 2011). As a result, it can sometimes be challenging to determine the exact building from which a picture was captured. In practice, additional spatial uncertainty was introduced because field pictures, although geotagged, were often taken from across the street or at a distance from the target buildings. Furthermore, pictures were captured using different devices with varying GPS accuracies, adding another layer of positional inaccuracy. The 25-m buffer adopted in the validation was selected to take all these uncertainties into account..

Additional sources of uncertainty include layover and PS positioning errors. Layover distortion, which is particularly significant in dense urban areas with tall buildings, can be quantified using the building height and the local incidence angle of the SAR signal. In the absence of airborne Light Detection and Ranging (LiDAR) data for the study area, layover effects were estimated based on reported building heights and the local incidence angle of the central pixel in the SAR images. Assuming an average building height of 12 m (Chaulagain et al., 2015; Ohsumi et al., 2016) and an incidence angle of 26.58 degrees, the average layover-affected area was estimated to be approximately 6 m. Furthermore, the PS positioning error is influenced by the accuracy of the DEM and the spatial resolution of the SAR sensor (Dörr et al., 2021), with errors for the CSK sensor typically ranging within a few meters, 2.7 m in the azimuth and 1 m in the slant range directions (Nitti et al., 2015). Although these distortions may occasionally cause adjacent buildings to be misidentified, the estimated error margins are small enough that field teams can easily compensate for them during on-site inspections.

Finally, the OSM database is not always complete and may lack some building footprints. Consequently, these missing buildings might not be included in the building-level analysis, even if field pictures were obtained for them. This might result in less positive correlations between field observations and buildings identified as having undergone significant changes during the reconstruction process. However, OSM has generally proven to be a reliable base map for urban studies, with several studies showing that its quality is comparable to that of official regional maps (Fan et al., 2014; Brovelli and Zamboni, 2018). Alternative datasets, such as Microsoft Building Footprints (Microsoft, 2025) and Open Buildings Data (Open Buildings, 2025) were evaluated but found to be either less accurate or in need of substantial modifications. OSM offered more precise building outlines, particularly for non-rectangular structures. We further validated OSM coverage against Google Earth VHR imagery and found no significant omissions. Therefore, despite its limitations, OSM remained the most appropriate and practical choice for our analysis.

While these uncertainties are present, integrating complementary datasets and techniques could mitigate their impact and enhance the overall robustness of the methodology. For example, Building Information Modelling (BIM) datasets, when available, offer detailed architectural information that can validate and enrich SAR-based observations. Alternative georeferencing approaches, such as aligning field photos with high-resolution optical imagery, can reduce GPS-related inaccuracies and improve the spatial accuracy of field validations. Moreover, incorporating ground-truth datasets such as structural health monitoring data, governmental reconstruction reports, or drone-based imaging, if available, can provide further validation data. Furthermore, using datasets from additional earthquake events and extended reconstruction phases could improve its generalisability and applicability across a broader range of scenarios. With sufficient labelled field data, integrating machine learning models into the methodology could be a valuable extension, as these models have demonstrated strong performance in automating classification tasks in remote sensing applications.

The core principle of the proposed method, detecting changes in the number of PSs using MT-InSAR, is scalable and adaptable to various disaster scenarios beyond earthquakes, such as floods, urban fires, and landslides. For instance, in the case of urban fires, severe damage or destruction of buildings leads to significant changes in radar backscatter, as affected structures lose the stability and surface characteristics needed for PS detection. The disappearance of these PSs in the time series serves as a clear indicator of fire-induced damage and subsequent reconstruction. This behaviour is directly observable through the proposed method and allows for effective post-fire building assessment. As long as a disaster results in substantial physical changes that impact radar reflectivity, the approach remains effective. While some adjustments, such as SAR data selection or temporal baseline tuning, may be necessary, the core concept is widely applicable.

Ultimately, the method provides systematic and scalable monitoring of urban areas in post-disaster scenarios, offering valuable insights for guiding field teams, prioritising reconstruction efforts, and assessing reconstruction progress over time. This ability to continuously track structural changes and reconstruction dynamics makes the method a valuable tool for long-term urban resilience planning. By analysing trends in building stability over multiple time periods, decision makers can better understand the pace of reconstruction and allocate resources more efficiently.

6. Conclusion

This study introduced a novel method for evaluating postearthquake building reconstruction. Using the MT-InSAR technique, we detected PSs linked to buildings by processing a time series of SAR data collected before and after the earthquake. A two-stage differential analysis was then performed to compare the number of PSs in pre- and post-event scenarios. The method begins with a regional assessment, analysing urban grid cells to identify areas affected by reconstruction after the earthquake. In areas showing the most significant changes, a more detailed building-level analysis was conducted to pinpoint specific buildings that had undergone reconstruction or remained collapsed years after the event. The approach highlights building locations where substantial changes have occurred, either from continued collapse or reconstruction. These identified locations can help guide field investigations at a regional scale to track reconstruction progress long after the earthquake.

The proposed method was applied to the 2015 Gorkha earthquake in Nepal using stacks of high-resolution CSK SAR images acquired before and after the event. Through the grid-level analysis, several urban areas showing significant changes were identified, prompting further investigation at the building level. Time-series pairs of different lengths were analysed, revealing that longer time series detected more changes related to reconstruction activities in the PS differential analysis. This is because longer time series can capture a broader range of activities over time, including debris accumulation, removal, and other phases of the reconstruction process. The building-level analysis identified specific locations where buildings had changed years after the earthquake, indicating buildings that remained collapsed, had been demolished, were under construction, or had been reconstructed.

Field observations collected in 2015 and during a return mission to Nepal in 2022 were used to validate the buildings identified by the PS differential analysis. The validation results confirmed that the method successfully located buildings that had undergone changes during the reconstruction phase, either remaining collapsed, being demolished, under construction, or reconstructed. The accuracy was higher when longer time series were used, suggesting a stronger correlation between the detected buildings and actual field observations. These results confirm the method's reliability in identifying locations affected by reconstruction activities, providing valuable target areas for future field surveys.

This study marks the first application of the MT-InSAR remote sensing technique to support extensive field investigations, particularly in the context of post-earthquake building reconstruction. It highlights the potential of MT-InSAR in identifying buildings impacted by reconstruction, offering a practical tool to identify locations that can be prioritised for field surveys. By doing so, this approach can significantly reduce the time and effort required for extensive investigations of building reconstruction progress across wide areas.

CRediT authorship contribution statement

Fatemeh Foroughnia: Validation, Formal analysis, Writing – original draft, Methodology, Data curation, Conceptualisation, Writing – review & editing, Visualisation, Investigation. Valentina Macchiarulo: Writing – review & editing, Conceptualisation, Methodology, Data curation. Pietro Milillo: Methodology, Data curation, Formal analysis, Writing – review & editing, Conceptualisation. Michael R.Z. Whitworth: Writing – review & editing, Data curation. Kenneth Gavin: Writing – review & editing, Supervision. Giorgia Giardina: Supervision, Resources, Data curation, Writing – review & editing, Methodology, Conceptualisation.

Funding

P.M. was funded by the National Aeronautics and Space Administration (NASA) under a contract with the Commercial Smallsat Data Scientific Analysis Program (NNH22ZDA001N-CSDSA), and the Decadal Survey Incubation Program: Science and Technology (NNH21ZDA001N-DSI).

Declaration of competing interest

The authors declare that they have no known competing financial interests or personal relationships that could have appeared to influence the work reported in this paper.

Acknowledgements

We thank the Italian Space Agency (ASI) for providing COSMO-SkyMed data (original COSMO-SkyMed product ASI Agenzia Spaziale Italiana (2009–2024)) for this project. We also thank the Earthquake Engineering Research Institute (EERI) and the Earthquake Engineering Field Investigation Team (EEFIT) for the validation pictures used in this study.

Appendix

See Figs. 10 and 11 and Tables 1-3.

Table 1Upper bound values of building area distributions for each pair, used in the building-level analysis.

Pairs	$\mathit{UB}\left(\mathit{area}_{\mathrm{bu}}\right)$
Pair 1	172
Pair 2	186.5
Pair 3	184

Table 2Number of buildings with over 50% change used for validation, categorised by pair and regions of interest.

Pairs	Kathmandu	Bhaktapur
Pair 1	1325	277
Pair 2	1186	323
Pair 3	2310	483

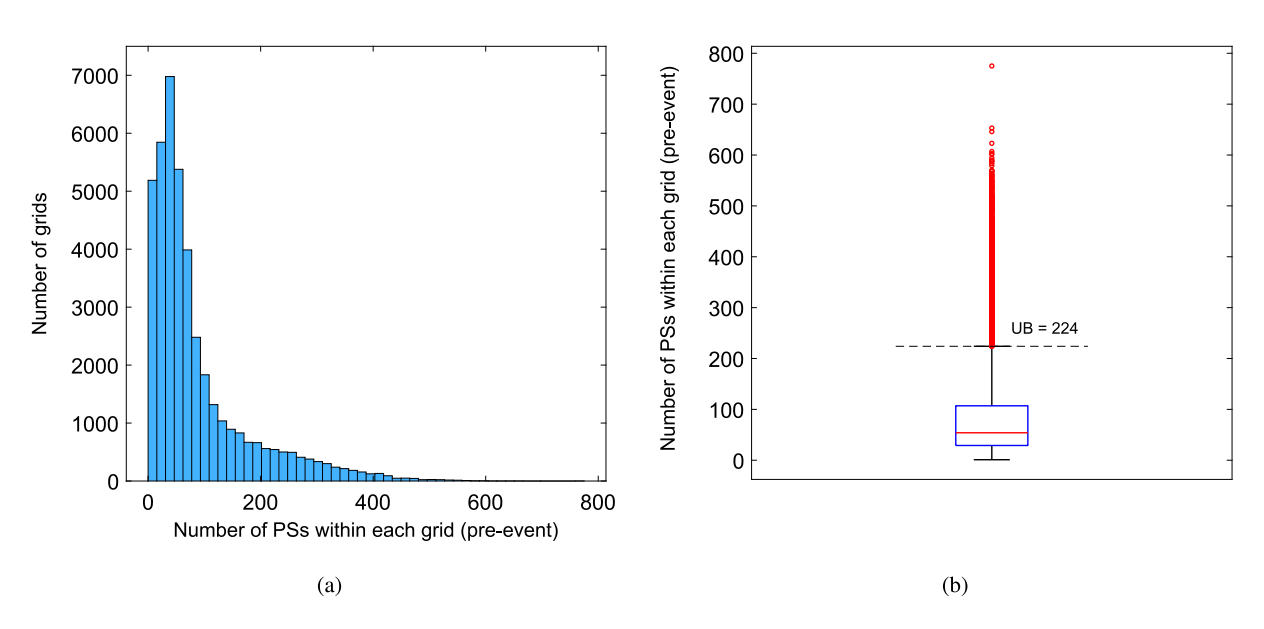


Fig. 10. Number of PSs per grid cell based on pre-event data: (a) histogram showing the frequency distribution and (b) box plot showing the variability of PS numbers (pre-event time series) per grid cell. The upper bound of the number of PSs (pre-event time series) used for grid-level analysis is 224.

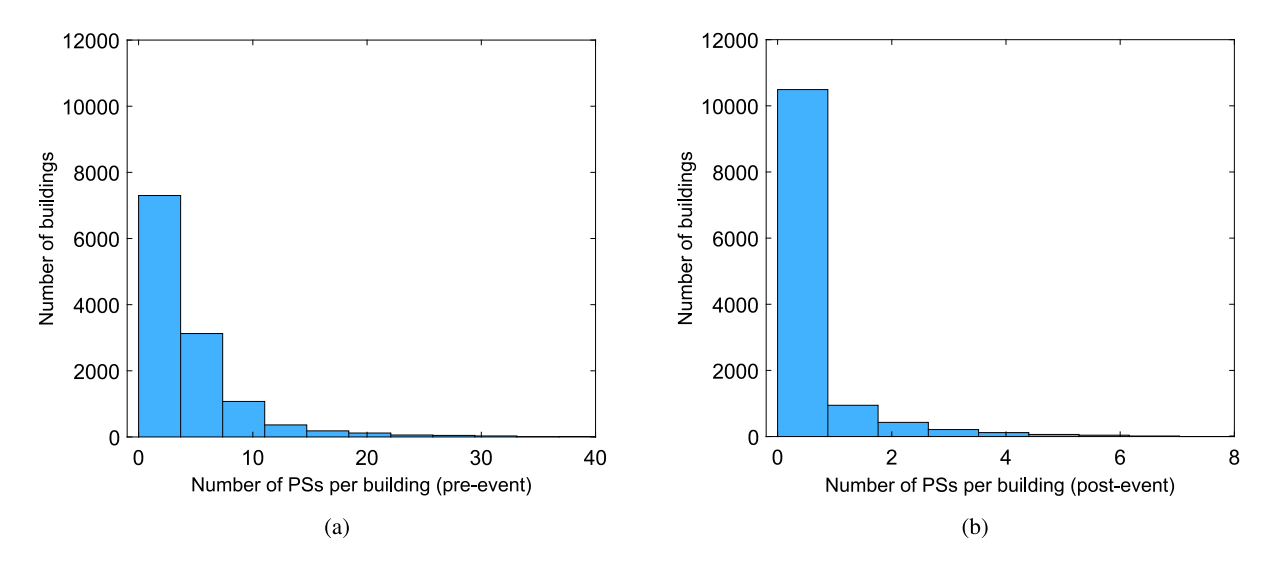


Fig. 11. Number of PSs per building footprint from the (a) pre-event and (b) post-event data (Post 3).

Table 3Perpendicular and temporal baselines with Doppler Centroid (DC) differences for the time series of Post 2.

Date	Perpendicular baseline (m)	Temporal baseline (days)	DC (Hz/PRF)
2015-05-15	-163.999841	91.256504	-0.088485
2015-05-19	-159.999831	58.357024	0.105961
2015-05-27	-151.999865	614.610937	0.113940
2015-06-04	-143.999851	-196.962032	0.104766
2015-06-20	-127.999869	-325.837476	0.097149
2015-07-06	-111.999926	486.776836	0.140111
2015-07-14	-103.999943	264.811148	0.092809
2015-07-18	-99.999979	1192.506395	-0.045642
2015-07-22	-95.999926	-123.844859	0.110280
2015-07-30	-87.999966	467.612367	0.119710
2015-08-03	-83.999945	-534.329165	-0.074591
2015-08-07	-79.999975	1109.278368	0.136659
2015-08-15	-71.999961	-221.292560	0.087761
2015-08-19	-67.999988	623.834242	-0.059247
2015-08-23	-63.999964	389.072153	0.143078
2015-09-04	-51.999982	188.979467	-0.072350
2015-10-26	0.000000	0.000000	0.050749
2015-12-29	63.999856	907.377859	0.127257
2016-03-02	127.999720	-80.828071	0.110878
2016-03-10	135.999689	48.072930	0.137601
2016-03-14	139.999700	-495.239130	-0.072549
2016-03-18	143.999674	-125.467680	0.102930
2016-03-26	151.999649	-456.710045	0.115239
2016-03-30	155.999628	87.576926	-0.044917
2016-04-11	167.999586	-148.616509	0.142271
2016-04-15	171.999568	165.720698	-0.043453
2016-04-19	175.999542	548.992779	0.105197
2016-04-27	183.999523	-158.426957	0.141159
2016-05-05	191.999515	-757.475284	0.121716
2016-05-13	199.999446	76.252961	0.101724
2016-05-17	203.999461	-919.418826	-0.057127
2016-05-21	207.999421	-168.595003	0.078637
2016-05-29	215.999390	-660.762455	0.115580

Data availability

The authors do not have permission to share data.

References

- Acharya, P., Sharma, K., Pokharel, G.R., Adhikari, R., 2022. Reviewing the progress of reconstruction five years after the 2015 Gorkha Earthquake, Nepal. Build. Res. Inf. 50 (6), 595–609.
- Ahmed, I., 2017. Resilient housing reconstruction in the developing world. In: March, A., Kornakova, M. (Eds.), Urban Planning for Disaster Recovery. Elsevier, Butterworth-Heinemann, pp. 171–188.
- Aktas, Y., So, E., Johnson, C., Donmez, K., Ozden, A., Parammal Vatteri, A., O'Kane, A., Kalkan, A., Andonov, A., Verrucci, E., et al., 2024. The Türkiye Earthquake Sequence of February 2023: A Longitudinal Study Report by EEFIT. Technical Report.
- Al-Khudhairy, D., Caravaggi, I., Giada, S., 2005. Structural damage assessments from IKONOS data using change detection, object-oriented segmentation, and classification techniques. Photogramm. Eng. Remote Sens. 71 (7), 825–837.
- Anniballe, R., Noto, F., Scalia, T., Bignami, C., Stramondo, S., Chini, M., Pierdicca, N., 2018. Earthquake damage mapping: An overall assessment of ground surveys and VHR image change detection after L'Aquila 2009 earthquake. Remote Sens. Environ. 210, 166–178.
- Bamler, R., 2000. Principles of synthetic aperture radar. Surv. Geophys. 21 (2–3), 147–157.
- Bevington, J., Pyatt, S., Hill, A., Honey, M., Adams, B., Davidson, R., Brink, S., Chang, S., Panjwani, D., Mills, R., et al., 2010. Uncovering Community Disruption using Remote Sensing: An Assessment of Early Recovery in Post-Earthquake Haiti. Technical Report, Disaster Research Center.
- Bianchini, S., Pratesi, F., Nolesini, T., Casagli, N., 2015. Building deformation assessment by means of persistent scatterer interferometry analysis on a landslide-affected area: The Volterra (Italy) case study. J. RS 7 (4), 4678–4701.
- Brovelli, M.A., Zamboni, G., 2018. A new method for the assessment of spatial accuracy and completeness of OpenStreetMap building footprints. ISPRS Int. J. Geo-Inf. 7 (8), 289.
- Brown, D., Saito, K., Liu, M., Spence, R., So, E., Ramage, M., 2012. The use of remotely sensed data and ground survey tools to assess damage and monitor early recovery following the 12.5. 2008 Wenchuan earthquake in China. Bull. Earthq. Eng. 10, 741–764.

- CEDIM, 2015. Nepal earthquakes report 3. URL: https://www.cedim.de/english/index. php.
- Chaulagain, H., Rodrigues, H., Spacone, E., Varum, H., et al., 2015. Seismic response of current RC buildings in Kathmandu Valley. Struct. Eng. Mech. 53 (4), 791–818.
- Ciampalini, A., Bardi, F., Bianchini, S., Frodella, W., Del Ventisette, C., Moretti, S., Casagli, N., 2014. Analysis of building deformation in landslide area using multisensor PSInSAR TM technique. Int. J. Appl. Earth Obs. Geoinf. 33, 166–180.
- Clinton, W.J., 2006. Lessons Learned from Tsunami Recovery: Key Propositions for Building Back Better. Office of the UN Secretary-General's Special Envoy for Tsunami Recovery, New York.
- Colesanti, C., Ferretti, A., Novali, F., Prati, C., Rocca, F., 2003. SAR monitoring of progressive and seasonal ground deformation using the permanent scatterers technique. IEEE Trans. Geosci. Remote Sens. 41 (7), 1685–1701.
- Contreras, D., Blaschke, T., Tiede, D., Jilge, M., 2016. Monitoring recovery after earth-quakes through the integration of remote sensing, GIS, and ground observations: The case of L'Aquila (Italy). Cartogr. Geogr. Inf. Sci. 43 (2), 115–133.
- Contreras, D., Forino, G., Blaschke, T., 2018. Measuring the progress of a recovery process after an earthquake: The case of L'aquila, Italy. Int. J. Disaster Risk Reduct. 28, 450–464.
- Crosetto, M., Monserrat, O., Cuevas-González, M., Devanthéry, N., Crippa, B., 2016.

 Persistent scatterer interferometry: A review. ISPRS J. Photogramm. Remote Sens. 115, 78–89.
- D'Aria, D., Ferretti, A., Guarnieri, A.M., Tebaldini, S., 2009. SAR calibration aided by permanent scatterers. IEEE Trans. Geosci. Remote Sens. 48 (4), 2076–2086.
- Derakhshan, S., Cutter, S.L., Wang, C., 2020. Remote sensing derived indices for tracking urban land surface change in case of earthquake recovery. J. RS 12 (5), 895.
- Dörr, N., Schenk, A., Hinz, S., 2021. Analysis of heterogeneous PS-InSAR derived subsidence rates using categorized GIS objects-a case study in the Mekong Delta. In: 2021 IEEE IGARSS. IEEE, pp. 2655–2658.
- EEFIT, 2019. EEFIT Mission Report: Gorkha, Nepal. Technical Report, EEFIT.
- EERI, 2015. Nepal earthquake clearinghouse. URL: https://learningfromearthquakes.org/2015-04-25-nepal/photo-gallery.
- Eghbali, M., Samadian, D., Ghafory-Ashtiany, M., Dehkordi, M.R., 2020. Recovery and reconstruction of schools after m 7.3 Ezgeleh-Sarpole-Zahab earthquake; part II: Recovery process and resiliency calculation. Soil Dyn. Earthq. Eng. 139, 106327.
- ESA, 2024. European space agency: COSMO-SkyMed full archive and tasking. URL: https://earth.esa.int/eogateway/catalog/cosmo-skymed-full-archive-and-tasking.
- Fan, H., Zipf, A., Fu, Q., Neis, P., 2014. Quality assessment for building footprints data on OpenStreetMap. IJGIS 28 (4), 700–719.

- Ferretti, A., Prati, C., Rocca, F., 2001. Permanent scatterers in SAR interferometry. IEEE Trans. Geosci. Remote Sens. 39 (1), 8–20.
- Foroughnia, F., Nemati, S., Maghsoudi, Y., Perissin, D., 2019. An iterative PS-InSAR method for the analysis of large spatio-temporal baseline data stacks for land subsidence estimation. Int. J. Appl. Earth Obs. Geoinf. 74, 248–258.
- Ge, P., Gokon, H., Meguro, K., 2020. A review on synthetic aperture radar-based building damage assessment in disasters. Remote Sens. Environ. 240, 111693.
- Ge, Y., Gu, Y., Deng, W., 2010. Evaluating China's national post-disaster plans: The 2008 Wenchuan earthquake's recovery and reconstruction planning. Int. J. Disaster Risk Sci. 1, 17–27.
- Giardina, G., Macchiarulo, V., Foroughnia, F., Jones, J.N., Whitworth, M.R., Voelker, B., Milillo, P., Penney, C., Adams, K., Kijewski-Correa, T., 2023. Combining remote sensing techniques and field surveys for post-earthquake reconnaissance missions. Bull. Earthq. Eng. 1–25.
- Goda, K., Kiyota, T., Pokhrel, R.M., Chiaro, G., Katagiri, T., Sharma, K., Wilkinson, S., 2015. The 2015 gorkha nepal earthquake: insights from earthquake damage survey. Front. Built Env. 1, 8.
- Goretti, A., Di Pasquale, G., 2004. Building inspection and damage data for the 2002 Molise, Italy, earthquake. Earthq. Spectra 20 (1_suppl), 167–190.
- Government of the Republic of Haiti, 2010. Action Plan for National Recovery and Development of Haiti: Immediate Key Initiatives for the Future. Technical Report, Government of the Republic of Haiti.
- Green, R., Miles, S., 2011. Social impacts of the 12 january 2010 Haiti earthquake. Earthq. Spectra 27 (1_suppl1), 447–462.
- Hanssen, R.F., 2001. Radar Interferometry: Data Interpretation and Error Analysis. Vol. 2, Springer Science & Business Media.
- Hashemi Parast, S.O., 2017. Application of Satellite Optical and SAR Imagery for Urban Reconstruction Monitoring and Land-Cover Classification in Arid Areas (Ph.D. thesis). Chiba University.
- Hashemi Parast, S.O., Yamazaki, F., Liu, W., 2017. Monitoring and evaluation of the urban reconstruction process in Bam, Iran, after the 2003 mw 6.6 earthquake. Nat. Hazards 85, 197–213.
- Hooper, A., Zebker, H., Segall, P., Kampes, B., 2004. A new method for measuring deformation on volcanoes and other natural terrains using InSAR persistent scatterers. Geophys. Res. Lett. 31 (23).
- Hoshi, T., Murao, O., Yoshino, K., Yamazaki, F., Estrada, M., 2014. Post-disaster urban recovery monitoring in pisco after the 2007 peru earthquake using satellite image. J. Disaster Res. 9 (6), 1059–1068.
- Italian Space Agency, 2019. COSMO-SkyMed mission and products description. Doc. N° ASI-CSM-PMG-NT-001, 8 July 2019, Issue 3.
- Jia, J., Ye, W., 2023. Deep learning for earthquake disaster assessment: Objects, data, models, stages, challenges, and opportunities. J. RS 15 (16), 4098.
- Kushiyama, Y., Matsuoka, M., 2019. Time series GIS map dataset of demolished buildings in Mashiki town after the 2016 Kumamoto, Japan earthquake. J. RS 11 (19), 2190.
- Livaoğlu, R., Timurağaoğlu, M.Ö., Serhatoğlu, C., Döven, M.S., 2018. Damage during the 6-24 february 2017 ayvacık (Çanakkale) earthquake swarm. NHESS 18 (3), 921-934.
- Lizundia, B., Shrestha, S.N., Bevington, J., Davidson, R., Jaiswal, K., Jimee, G.K., Kaushik, H., Kumar, H., Kupec, J., Mitrani-Reiser, J., et al., 2016. EERI Earthquake Reconnaissance Team Report: M7. 8 Gorkha, Nepal Earthquake on April 25, 2015 and its Aftershocks. Technical Report, EERI, Oakland, CA, USA.
- Lu, Y., Xu, J., 2015. Comparative study on the key issues of postearthquake recovery and reconstruction planning: Lessons from the United States, Japan, Iran, and China. Nat. Hazards Rev. 16 (3), 04014033.
- Lyons, M., Schilderman, T., Boano, C., 2010. Building Back Better: Delivering People-Centred Housing Reconstrution at Scale. Practical Action Pub..
- Macchiarulo, V., Giardina, G., Milillo, P., Aktas, Y.D., Whitworth, M.R., 2024. Integrating post-event very high resolution SAR imagery and machine learning for building-level earthquake damage assessment. Bull. Earthq. Eng. 1–27.

- Macchiarulo, V., Milillo, P., Blenkinsopp, C., Reale, C., Giardina, G., 2021. Multitemporal InSAR for transport infrastructure monitoring: Recent trends and challenges. In: PROC INST CIV ENG-BR.. Vol. 176, Thomas Telford Ltd, pp. 92–117.
- Mannakkara, S., Wilkinson, S., Francis, T.R., 2014. Build back better" principles for reconstruction. Ency. Earthq. Eng. 1–12.
- Matin, S.S., Pradhan, B., 2022. Challenges and limitations of earthquake-induced building damage mapping techniques using remote sensing images-a systematic review. Geocarto Int. 37 (21), 6186–6212.
- Microsoft, 2025. Global ML building footprints. URL: https://github.com/microsoft/ GlobalMLBuildingFootprints.
- Miura, H., Midorikawa, S., Matsuoka, M., 2016. Building damage assessment using high-resolution satellite SAR images of the 2010 Haiti earthquake. Earthq. Spectra 32 (1), 591–610.
- Nitti, D.O., Nutricato, R., Lorusso, R., Lombardi, N., Bovenga, F., Bruno, M.F., Chiaradia, M.T., Milillo, G., 2015. On the geolocation accuracy of COSMO-SkyMed products. In: SAR Image Analysis, Modeling, and Techniques XV. Vol. 9642, SPIE, pp. 69–80.
- Ohsumi, T., Mukai, Y., Fujitani, H., 2016. Investigation of damage in and around kathmandu valley related to the 2015 Gorkha, Nepal earthquake and beyond. Geotech. Geol. Eng. 34, 1223–1245.
- Omidvar, B., Zafari, H., Derakhshan, S., 2010. Reconstruction management policies in residential and commercial sectors after the 2003 bam earthquake in Iran. Nat. Hazards 54, 289–306.
- Open Buildings, 2025. Open buildings. URL: https://sites.research.google/gr/open-buildings.
- OpenStreetMap, 2023. URL: https://www.openstreetmap.org.
- Perissin, D., Wang, T., 2011. Repeat-pass SAR interferometry with partially coherent targets. IEEE Trans. Geosci. Remote Sens. 50 (1), 271–280.
- Perissin, D., Wang, Z., Wang, T., 2011. The SARPROZ InSAR tool for urban subsidence/manmade structure stability monitoring in China. In: Proceedings of the ISRSE. Vol. 1015, Sidney, Australia.
- Platt, S., Brown, D., Hughes, M., 2016. Measuring resilience and recovery. Int. J. Disaster Risk Reduct. 19, 447–460.
- Platt, S., Gautam, D., Rupakhety, R., 2020. Speed and quality of recovery after the gorkha earthquake 2015 nepal. Int. J. Disaster Risk Reduct. 50, 101689.
- Polese, M., Di Ludovico, M., Prota, A., 2018. Post-earthquake reconstruction: A study on the factors influencing demolition decisions after 2009 L'Aquila earthquake. Soil Dyn. Earthq. Eng. 105, 139–149.
- USGS, 2015. M 7.8 67 km NNE of Bharatpur, Nepal. URL: https://earthquake.usgs.gov/earthquakes/eventpage/us20002926/executive.
- Van Leijen, F.J., 2014. Persistent scatterer interferometry based on geodetic estimation theory.
- Voelker, B., Milillo, P., Tavakkoliestahbanati, A., Macchiarulo, V., Giardina, G., Recla, M., Schmitt, M., Cescon, M., Aktas, Y.D., So, E., 2024. The EEFIT remote sensing reconnaissance mission for the february 2023 Turkey earthquakes. IEEE J. Sel. Top. Appl. Earth Obs. Remote. Sens..
- Westoby, L., Wilkinson, S., Dunn, S., 2021. The road to recovery: Understanding the challenges affecting school reconstruction in rural nepal following the 2015 Gorkha earthquake. Int. J. Disaster Risk Reduct. 56, 102120.
- Whitworth, M., 2023. Shared knowledge on earthquake recovery and reconstruction:
 The nepal EEFIT 2022 return mission. In: Proc. SECED Conf. Earthq. Eng. Dyn.
 Sustain. Future..
- Wilkinson, S., DeJong, M., Novelli, V., Burton, P., Tallet-Williams, S., Whitworth, M., Guillermo, F., White, T., Trieu, A., Ghosh, B., Datla, S., 2019. The Mw 7.8 Gorkha, Nepal Earthquake of 25 April 2015: A Field Report by EEFIT. Technical Report, EEFIT.
- Wu, S., Zhang, B., Ding, X., Shahzad, N., Zhang, L., Lu, Z., 2022. A hybrid method for MT-InSAR phase unwrapping for deformation monitoring in urban areas. Int. J. Appl. Earth Obs. Geoinf. 112, 102963.
- Zandbergen, P.A., Barbeau, S.J., 2011. Positional accuracy of assisted GPS data from high-sensitivity GPS-enabled mobile phones. J. Navig. 64 (3), 381–399.